19

Nuclear magnetic resonance gyroscopes

E. A. Donley and J. Kitching

19.1 Introduction

Gyroscopes measure rotation of a platform with respect to an inertial system [1]. The classic example of a mechanical gyroscope is a spinning massive object in a gravitational field, with one point of the object on its rotation axis held fixed. In this system, rotation ("precession") about the gravitational field axis will be observed at a rate proportional to the field magnitude and inversely proportional to the angular momentum of the object. Changes in the precession frequency indicate rotation with respect to inertial space.

As described in previous chapters, atomic spins in a magnetic field precess in a manner analogous to spinning mechanical systems in a gravitational field, with the precession rate proportional to the field magnitude and inversely proportional to the atom's angular momentum. Rotation of a measurement platform within the inertial frame can be detected by monitoring the apparent change in the Larmor frequency of the atoms.

In an inertial frame, the equation of motion for the spin polarization $\mathbf{P}$ of an ensemble of spins is $\partial\mathbf{P}/\partial t = \gamma\mathbf{B} \times \mathbf{P}$. When the laboratory frame containing the instruments used to measure the Larmor precession is rotating with respect to inertial space, the Larmor frequency is shifted by Ω, the rotation rate of the apparatus about the direction of the applied field. In this case, the equation of motion for $\mathbf{P}$ becomes

$$\frac{\partial \mathbf{P}}{\partial t} = (\Omega + \gamma\mathbf{B}) \times \mathbf{P}. \tag{19.1}$$

The concept of rotation sensing by a measurement of the Larmor frequency is illustrated in Fig. 19.1.

The problem therefore becomes one of measuring the rotation-induced precession-frequency shift with high precision, while simultaneously controlling all other effects that lead to precession-frequency shifts. Electrons (and atoms with a single valence electron

Optical Magnetometry, ed. Budker, D. and Jackson Kimball, D. F. Published by Cambridge University Press.

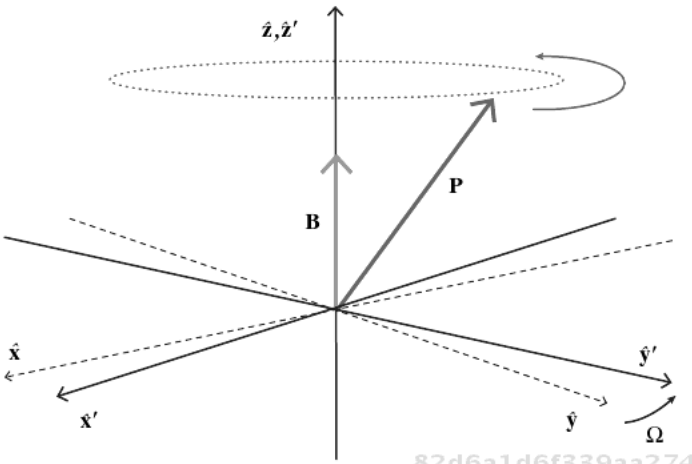

Figure 19.1 Determining rotation rate based on a measurement of the Larmor frequency. Here the laboratory frame is shown as the $(\hat{\mathbf{x}}', \hat{\mathbf{y}}', \hat{\mathbf{z}}')$ coordinate system and the inertial coordinate system is shown as $(\hat{\mathbf{x}}, \hat{\mathbf{y}}, \hat{\mathbf{z}})$. The magnetic field $\mathbf{B}$ is applied along the $\hat{\mathbf{z}}$-axis in both coordinate systems. $\mathbf{P}$ precesses in the $(\hat{\mathbf{x}}, \hat{\mathbf{y}}, \hat{\mathbf{z}})$ coordinate system with the "absolute" frequency γB. The lab frame, which contains the lasers and coils that measure the precession frequency, is rotating about the magnetic field with respect to the inertial frame at a frequency Ω. In transforming the precession from the inertial to the laboratory frame, the observed frequency is shifted by Ω.

whose magnetic moment is dominated by the electron magnetic moment) precess in a magnetic field at rate of approximately 1 MHz/G. Atoms with closed electron shells have a magnetic moment dominated by the nucleus, and typically precess 1000 times more slowly. A nuclear magnetic resonance gyroscope (NMRG) is one based on the precession of nuclear magnetic moments.

Table 19.1 summarizes the nuclear spin angular momentum values, gyromagnetic ratios, and nuclear quadrupole moments for several isotopes that have been used in NMR gyroscopes. Also included is an effective field for a rotation rate of 1°/h as determined by γ.[1] Larger values of γ put stricter requirements on the field stability in order to reach the same level of rotation-rate uncertainty. Table 19.1 also gives the gyromagnetic ratios for bare electrons as well as for ^{87}Rb in weak fields. For a free electron, γ is equal to the magnetic moment divided by the spin angular momentum. For an electron bound to a nucleus, γ is reduced by a factor of $1/q$, where $q = 2I + 1$ is the nuclear slowing-down factor, and I is the nuclear spin.

The most established gyroscope application is inertial navigation, in which the position of a moving platform is determined from quasi-continuous monitoring of the platform acceleration and rotation. To get a sense of the requirements for gyroscope performance, one can consider an example requiring high-performance inertial navigation. For a platform

[1] 1°/h is the minimum resolution needed for short-flight navigation applications, see Table 19.2.

Table 19.1. *Nuclear spin, gyromagnetic ratio, and the effective field equivalent to a 1°/h rotation frequency for atoms commonly used in NMR gyroscopes [2]. The final column contains the nuclear quadrupole moment, Q_n. For comparison, data for electron paramagnetic resonance (EPR) species are also shown.*

NMR species	I (h)	γ (MHz/T)	B_{eff} for 1°/h (fT)	Q_n (fm^2)
^{3}He	1/2	−32.44	23.8	
^{21}Ne	3/2	−3.363	229	10.16
^{83}Kr	9/2	−1.644	469	25.9
^{129}Xe	1/2	−11.86	65.1	
^{131}Xe	3/2	3.516	219	−11.4
^{199}Hg	1/2	7.712	100	
^{201}Hg	3/2	−2.847	271	38.6
EPR species		γ (MHz/T)	B_{eff} for 1°/h (fT)	
e^-		28030	0.028	
^{87}Rb	3/2	6998	0.110	

Table 19.2. *Required gyroscope uncertainty for navigation applications [3].*

Gyroscope uncertainty °/h	Systems applications
> 10	Automotive sensing
1	Attitude heading, short-flight devices
0.1	Some aircraft
0.01	Commercial airliners
< 0.001	Ships, submarines, spacecraft

moving at 800 km/h, inertial positioning of the platform to within 1 km over 2000 km of movement requires a rotation uncertainty of order $2\pi \times 10^{-8}$ rad/s, or 0.01°/h. This is equivalent to a magnetic field uncertainty of about 10 fT for nuclear species and 10 aT for electrons. A gyroscope based on alkali electronic spin precession alone would put very strict requirements on the magnetic-field stability, which is why NMR is the method of choice for spin-based gyroscopes. Nuclear spins also tend to have long coherence times since they interact only weakly with their environment. Table 19.2 summarizes the required gyroscope uncertainty for several navigation applications.

The operation of most NMR gyroscopes can be thought of as proceeding in three distinct steps: first the nuclear spins are polarized; then they are allowed to precess/rotate about the magnetic field direction during which time the rotation information is encoded in the spin orientation; finally the spin orientation is read out. Often these three steps happen simultaneously and continuously.

The nuclei of some atoms (such as ^{199}Hg or ^{201}Hg) can be polarized through direct optical pumping with resonant circularly polarized light. The orientation of the nuclei after precession can be detected in a similar manner. The earliest implementations of NMR gyroscopes were based on Hg atoms. More frequently, the nuclei of other atoms (noble gases, in particular) can be polarized through spin-exchange collisions with another optically polarized species, such as alkali atoms, contained in the same cell. In this case, the alkali atoms can also be used as an in situ magnetometer to read out the polarization orientation of the noble gas through its effective magnetic field.

A more detailed description of the NMR gyroscope based on spin-exchange optically pumped noble-gas nuclei is as follows. A vapor cell contains one or more noble-gas isotopes with nonzero nuclear spin (such as ^{129}Xe and ^{131}Xe), and an alkali metal (such as ^{87}Rb). Circularly polarized light resonant with an optical transition polarizes the alkali species, and the alkali electronic spin polarization is transferred to the noble-gas nuclei through collisions via spin-exchange optical pumping [4]. The alkali and noble-gas spins are continuously driven at their respective resonant frequencies and they precess about an applied magnetic field. In addition to the applied field, the alkali spins sense a field arising from the noble-gas polarization such that the total field as sensed by the alkali atoms rotates on a cone centered on the static field at the noble-gas precession frequency. All of the precession frequencies can be measured by analyzing the signal of a transverse probe beam that senses the direction of the alkali spin polarization.

Over short measurement times, noise processes inherent to the NMR gyroscope system generate an angle random walk (ARW), or white frequency noise, in the rotation rate. The rotation rate uncertainty of an NMR gyroscope due to this white frequency noise is determined by the transverse nuclear spin relaxation time, T_2, the measurement time, τ, and the measurement signal-to-noise ratio averaged over a time T_2 (S/N) [5, 6]:

$$\delta\Omega \sim \frac{1}{T_2(\mathrm{S/N})\sqrt{\tau/T_2}}. \tag{19.2}$$

This can be understood as follows. The linewidth of the transition is given by the inverse of the relaxation time. This line can be resolved over a measurement time T_2 to a statistical fractional uncertainty given by the measurement signal-to-noise ratio. Repeated measurements over a time τ improve the resolution further by an amount $\sqrt{\tau/T_2}$. The ARW noise specification for an NMR gyroscope is determined from the rotation rate statistical uncertainty as ARW = $\delta\Omega\sqrt{\tau}$, and is usually specified in the units of degrees per root hour.

In the case of a spin-exchange optically pumped NMR gyroscope, it is useful to view the signal-to-noise ratio as being equal to the magnetic field produced by the noble-gas nuclei as seen by the alkali atoms divided by the sensitivity of the alkali magnetometer. Thus, a

high noble-gas density, large polarization fraction, and high-precision measurement of the induced magnetic field lead to improved rotation sensing.

The bias instability expresses the limit of the gyroscope uncertainty on long time scales as determined by drift, $1/f$ noise and other non-Gaussian or nonstationary noise processes. For NMR gyroscopes, the most critical factor influencing the bias instability is the extent to which the magnetic field can be controlled, since changes in this parameter are indistinguishable from changes in rotation rate for a single atomic species. An elegant and powerful technique for reducing the effects of magnetic-field instability is to introduce a second noble-gas species, with a gyromagnetic constant different from the first, into the cell. In this configuration, changes in magnetic field cause different frequency shifts for the two species, while rotations cause identical shifts. As a result, the effects of changing magnetic fields can be separated from the true rotation signal and the bias instability from field changes is reduced. This method is discussed in more detail in Section 19.4. A second method for reducing the effects of magnetic fields, the alkali–noble-gas comagnetometer is discussed in Section 19.5.

A second important factor influencing bias instability is the effect of the nuclear electric quadrupole moment. Atomic nuclei are not perfectly round, and the nonspherical electric charge distribution interacts with electric field gradients (for example near the wall of the container) to produce a shift in the precession frequency. The effects of these shifts are discussed in more detail in Section 19.2.2.

The first proposals for NMR gyroscopes appeared in the 1950s [7, 8]. Optically pumped NMR gyroscopes were introduced in the 1960s with the advent of gyroscopes based on mercury nuclei [9] and continued into the 1980s with the development of NMR gyroscopes based on the noble gases [10]. Work on NMR gyroscopes mostly stopped in the 1980s, but NMR gyroscopes have seen a revival recently, in part because of advances in microfabrication and laser technology, and also because of the development of new NMRG methods based on comagnetometry [11].

19.2 NMR frequency shifts and relaxation

As with most resonant instruments, relaxation of the NMR spin resonance plays a critical role in determining the gyroscope short-term instability or ARW. The closely related issue of shifts in the NMR resonant frequency affects the bias instability and offset. In this section, we discuss the physical phenomena that underlie relaxation and frequency shifts in NMR gyroscopes.

Note that in the following, we generally speak of relaxation in terms of the longitudinal spin relaxation time T_1. The extent to which T_1 is dominated by spin-exchange collisions determines the signal-to-noise ratio, since it determines the achievable noble-gas polarization through spin-exchange optical pumping. T_1 also provides an upper bound on the transverse relaxation time T_2, which determines the ARW, with T_2 being reduced from T_1 by effects like random field fluctuations.

19.2.1 Spin exchange

Spin exchange [2] is an interaction between two atoms in which angular momentum is conservatively transferred from one atom to the other through a collision. Spin exchange can occur between atoms of the same species or of different species and typically results in a change in the equilibrium polarization of the ensemble, as well as both relaxation and a shift of one or both resonance frequencies.

When one atomic species, polarized through optical pumping, interacts with a second atomic species, the second species can become polarized. This is known as spin-exchange optical pumping (SEOP), and is one of the many interesting and useful effects that arise from spin-dependent interactions in atomic samples. A review of spin-dependent interactions can be found in [2].

SEOP in alkali–noble-gas mixtures occurs through binary collisions, as well as through the formation of van der Waals molecules through three-body collisions [12, 13]. The third body can either be a buffer-gas molecule, like N_2, or another noble-gas atom if the noble-gas density is sufficiently high [14].

For binary collisions, the longitudinal spin-relaxation rate can be written simply as the product of the alkali density n_{al}, a spin-exchange cross-section, σ, and the mean relative thermal velocity $\bar{v} = \sqrt{8k_BT/\pi \mathrm{m}}$, where m is the reduced mass in the alkali–noble-gas collision [15]. The longitudinal spin-relaxation rate from the formation of van der Waals molecules is inversely proportional to the noble-gas density and is characterized by the rate γ_V. Combining the effects of binary collisions and van der Waals molecule formation, the spin relaxation rate is [12, 14]

$$\frac{1}{T_1} = n_{\mathrm{al}}\left(\frac{\gamma_V}{n_{\mathrm{ng}}} + \sigma v\right) + \gamma' = R_{\mathrm{se}} + \gamma'. \tag{19.3}$$

Here, n_{ng} is the noble-gas number density and γ' is the relaxation rate from mechanisms other than spin exchange, which includes effects from wall collisions and magnetic field gradients.

Binary collisions dominate the longitudinal spin-exchange rate for the lighter noble gases, but the formation of van der Waals molecules can play a dominant role for heavy noble gases such as Xe, and can significantly shorten the period required to spin-polarize the noble-gas nuclei. At high noble-gas and/or buffer-gas densities, the lifetime of the weakly bound van der Waals molecules can be reduced to the point that the molecules do not live long enough for spin exchange to occur efficiently [12], and the spin-exchange rate due to binary collisions can exceed the spin-exchange rate due to van der Waals molecules [14].

The equilibrium noble-gas polarization can be expressed in terms of the alkali–noble-gas spin exchange rate R_{se}, the equilibrium spin polarization of the alkali atoms, P^{e}, and γ', as

$$P^{\mathrm{ng}} = P^{\mathrm{e}}\frac{R_{\mathrm{se}}}{R_{\mathrm{se}} + \gamma'}. \tag{19.4}$$

Spin-exchange also causes frequency shifts in each interacting species, which are manifest as an apparent enhancement of the magnetic field arising from the magnetization of the spin-exchange partner. The enhancement is caused by the hyperfine contact interaction [16, 17], which arises from an attraction between the alkali electron and the noble-gas nucleus. This effect enhances the ability for in situ alkali magnetometry to sense the noble-gas magnetization, since the field generated by the noble-gas nuclei can be magnified by orders of magnitude over what would be expected classically [18].

Expressed as an effective magnetic field arising from the polarization $\mathbf{P}$ of the other species, we can write an effective magnetic field

$$\mathbf{B}_{\text{eff}} = \frac{8\pi\kappa_0}{3}\mathbf{M} = \frac{8\pi\kappa_0}{3}\mu n\mathbf{P}. \tag{19.5}$$

Here $\mathbf{M} = \mu n\mathbf{P}$ is the magnetization of the other species, μ is the magnetic moment, n is the density, and κ_0 is the spin-exchange enhancement factor. Spin-exchange shifts were studied in detail in [19], and estimates of κ_0 were made in [15]. The enhancement κ_0 tends to be larger for the heavier noble gases. Depending on the alkali species, κ_0 ranges from $6 < \kappa_0 < 10$ for ^{3}He to $300 < \kappa_0 < 900$ for ^{129}Xe, with the higher values for a particular noble-gas nucleus corresponding to the heavier alkali atoms.

While the enhanced magnetic field improves NMRG sensitivity, spin-exchange also causes magnetization-dependent shifts of the NMR resonances that depend on cell temperature and laser power. A method of removing NMRG bias instability introduced by drifts in the alkali polarization was proposed in [20], and would require the use of three noble-gas isotopes instead of two. The shift is proportional to the alkali polarization, and having measurements of three Larmor frequencies allows for cancelation of the shift.

19.2.2 Quadrupole surface frequency shifts

Nuclei that have electric quadrupole moments are affected by electric-field gradients, which can cause relaxation and shifts of the NMR frequency. The magnitude of such shifts is proportional to the dot product between the electric field gradient and the nuclear quadrupole moment, Q_n. All nuclei that have a nuclear spin of $I > 1/2$ have nuclear quadrupole moments; these nuclei include ^{201}Hg and all $I \neq 0$ noble gases except for ^{3}He and ^{129}Xe (see Table 19.1). For all of the demonstrated dual-isotope NMR gyroscopes referenced below (Section 19.4), at least one of the NMR isotopes has a nuclear quadrupole moment.

In the limit where the nuclear quadropole resonance (NQR), shifts are small compared to the Zeeman shifts, the NQR interaction causes each NMR line to split into an array of $2I$ lines (Fig. 19.2). A nucleus with $I = 3/2$, for example, has four Zeeman energy levels. Three $\Delta m = 1$ transitions are allowed. When the electric-field gradient is zero, all the transitions between the Zeeman levels have the same frequency. However, when an electric field gradient is present, nonidentical shifts of the Zeeman energy levels result in a line triplet, with the spacing between the lines determined by the mean quadrupole interaction energy. The NQR shift also depends on the relative orientation of the principal axis of the

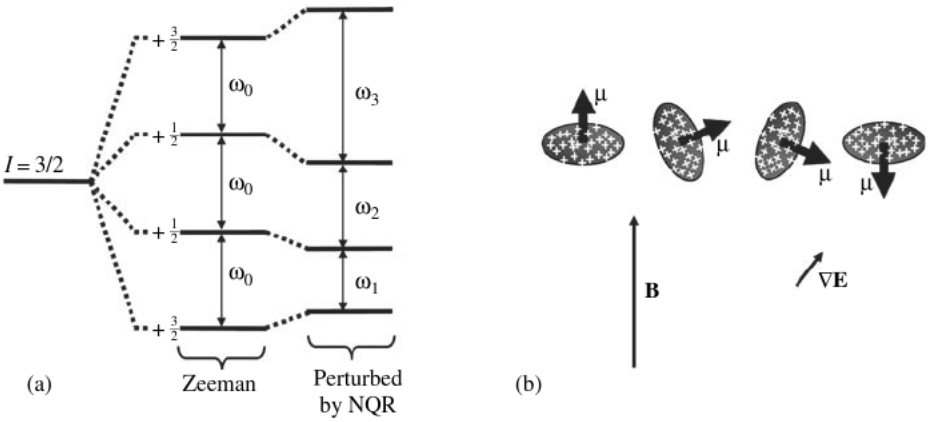

Figure 19.2 (a) Shifts of the Zeeman lines for an $I = 3/2$ nucleus perturbed by a weak electric-field gradient. (b) Pictorial view of the states of the nucleus in the fields. Nuclear quadrupole moments arise from asphericity of the nuclear charge distribution.

electric field gradient (a tensor) and the magnetic field axis, and it vanishes at the "magic angle" of 54.7°. Without careful experimental design, NQR interactions shift the lines and complicate the NMR spectrum.

For gases in vapor cells, electric-field gradients can arise through distortions in the electron cloud that occur during wall collisions [21], with the size of the NQR shift being proportional to the time-averaged electric-field gradient. The averaged electric-field gradients vanish for spherical and cubic cells; however, significant electric-field gradients can arise in cells with asymmetries in their shape or material construction. Smaller cells, all else being equal, result in more wall collisions and a correspondingly larger NQR shift.

Early studies on NQR shifts were performed for ^{83}Kr [22], ^{201}Hg [23, 24], and ^{131}Xe [25]. In these studies, the sample cells were nearly spherically symmetric. The shifts caused line broadening and low-frequency beating of the NMRG signals but were not large enough to be well resolved.

An enhancement of $\sim 100\times$ in the size of the shifts was demonstrated by use of highly asymmetric cells [26], which allowed for clear resolution of the NQR lines in ^{131}Xe. A detailed microscopic theory of the wall interactions was also developed [27] and compared to measurements of the NQR splittings versus cell asymmetry [28]. In the asymmetric cells, collisions with the walls along the axis of the narrower cell dimension are more frequent than collisions with the walls along the other directions, which results in a large average electric-field gradient. The large NQR interactions allowed for detailed quantitative studies of the electric-field gradients and the activation energies for surface adsorption. Similar studies with asymmetric cell shapes were later performed on ^{131}Xe [29] and ^{83}Kr [30]. NQR shifts for ^{201}Hg have also been studied in detail in the context of precision-measurement tests of spatial isotropy [31, 32].

NQR resonances of ^{131}Xe in the limit of zero applied magnetic field and deviations from Berry's adiabatic geometric phase under rotation have also been studied [33]. The studies were performed in a highly asymmetric cylindrical cell of 2 cm diameter and 2 mm height. In this regime, the NQR shifts were larger than the Zeeman frequency, and mixing of the nuclear spin energy levels through rotation made all six transitions between nuclear energy levels allowed ($\Delta m = 1$, 2, and 3).

More recently, an NQR study on ^{131}Xe nuclei in a microfabricated cell of 1 mm^3 volume was performed [34]. Although the cells had cubic symmetry, the NQR shifts were larger than the Zeeman frequency for magnetic fields of less than 50 nT. The strong electric-field gradient ($\sim$30 GV/cm^2) was generated by anisotropy in the cell-wall materials as opposed to the cell shape, since two of the cell walls were formed of borosilicate glass and four of the cell walls were formed of silicon.

19.2.3 General wall relaxation

Even for nuclei that do not have a nuclear quadrupole moment (^{3}He and ^{129}Xe), relaxation from wall collisions can limit the longitudinal spin lifetime, particularly for small cells. The mechanisms for this relaxation are poorly understood at present [2], but wall relaxation is stronger when atoms spend a longer time adhered to the cell wall during wall collisions. The wall relaxation rate is inversely proportional to the cell diameter [2], and decreases exponentially with increasing temperature, since the wall-adhesion time also decreases.

The use of buffer gases can slow the rate of diffusion across the cell and reduce the relaxation rate from wall collisions. Silicone- and hydride-based wall coatings can also be used to lower the adhesion time and the wall-relaxation rate [35, 36]. Borosilicate is commonly used for glass-blown cells because of the relative ease with which it can be blown. More exotic cell-wall materials like aluminosilicate can also be used to minimize wall relaxation, particularly for ^{3}He, for which other relaxation rates are very low [37]. The He diffusivity in aluminosilicate is orders of magnitude lower than in borosilicate such that the ^{3}He wall adhesion time on aluminosilicate is much shorter.

19.2.4 Magnetic-field gradients

The spatial diffusion of atoms in the presence of inhomogeneous magnetic fields is another important source of relaxation [17, 38, 39]. At high pressures, when the spin precession period is short compared to the cell diffusion period, the longitudinal relaxation rate arising from gradients can be expressed as [17]

$$\frac{1}{T_1} = D\frac{|\nabla B|^2}{B_z^2}. \tag{19.6}$$

The resulting relaxation can be reduced by applying a large uniform bias field, B_z. D is the diffusion constant, which is inversely proportional to the pressure.

At low pressures, when the diffusion period is much shorter than the spin precession period, the longitudinal relaxation rate is proportional to the pressure and motional narrowing is observed [39].

Field gradients can arise from sources external to the cell as well as from the alkali and noble-gas atoms in the cell. For cells that are perfect spheres, the self-field as sensed by the nuclear spins is zero, and the field arising from the uniform magnetization of the alkali atoms is constant. For cells that are not spherical, the nuclei can sense gradients from both their own polarization and the alkali polarization [40]. Field gradients from cell asphericity can be the primary limit on the longitudinal relaxation rate of ^{3}He, for which relaxation rates from other mechanisms can be small. For small cells, effective field gradients from gradients in the alkali polarization can be significant because of depolarizing wall collisions.

19.2.5 Noble-gas self-relaxation

Self-relaxation of the nuclear polarization also occurs through self-collisions, and the mechanism for the relaxation depends on the isotope under study. Noble-gas electron clouds are distorted during noble-gas self-collisions, and these distortions produce electric-field gradients. For $I > 1/2$ isotopes, the interaction between the induced electric-field gradients and the nuclear quadrupole moments generate torques on the spins that cause longitudinal relaxation. The relaxation rate is proportional to the noble-gas pressure, and can be the dominant relaxation mechanism for $I > 1/2$ isotopes – particularly at high noble-gas pressure, and in large cells where the wall effects are relatively weaker. Quadrupolar relaxation from self-collisions can be significant for any NMR gyroscope that uses an isotope that has a nuclear quadrupole moment.

Quadrupolar relaxation causes the maximum achieved noble-gas polarization in optical-pumping experiments to depend on the noble-gas partial pressure [41, 42]. In large cells, the quadrupolar relaxation rate for ^{131}Xe is proportional to the noble-gas density, with the proportionality constant 3.96×10^{-2} amagat^{-1} s^{-1} [42],[2] which limits the spin lifetime to 25 s for a 1-amagat ^{131}Xe sample. For ^{21}Ne, the relaxation rate is much lower, and the lifetime as limited by quadrupolar relaxation is 210 minutes for a 1-amagat sample [43].

For ^{3}He, which does not have a nuclear quadrupole moment ($I = 1/2$), self-relaxation from dipole–dipole interactions can dominate the longitudinal spin relaxation in carefully prepared spherical sample cells. When dipolar spin relaxation is the limiting factor for the spin lifetime, the lifetime can be as long as 75 h for a 10 amagat ^{3}He sample [44].

For ^{129}Xe self-collisions, the dipole–dipole interaction is negligible, and bulk relaxation times are limited by the collisional spin–rotation interaction to 55 h for a 1-amagat sample [4].

[2] The amagat is defined as the ideal-gas density at standard temperature and pressure.

19.3 Alkali shifts and relaxation mechanisms

Many varieties of NMR gyroscopes depend on alkali atoms for optical pumping and/or detection of the magnetic field produced by the noble gas; therefore the S/N ratio depends strongly on the relaxation mechanisms and frequency shifts that affect the alkali atoms. Since these effects are reviewed in detail in Chapters 1–6 and 10–12, they are mentioned only briefly here.

At low alkali densities, the alkali relaxation is usually dominated by a combination of wall collisions and collisions with any buffer gas (including the NMR gas) in the cell. Since the wall-induced relaxation rate is inversely proportional to the buffer gas pressure, while the buffer-gas-induced relaxation rate is proportional to the pressure, an optimum pressure occurs for any given cell size [45] (see also Chapter 7).

Naturally, better signal-to-noise ratios for the measurement of magnetic fields are obtained with higher densities of alkali atoms because of statistical averaging of a larger number of atoms. However, at higher alkali densities, spin-exchange collisions between alkali atoms usually limit the relaxation time. In certain regimes of operation (notably for the comagnetometer approach described below), alkali–alkali spin-exchange-relaxation can be strongly suppressed. This spin-exchange-relaxation-free (SERF) operation [46–50] allows much higher magnetic field sensitivities to be achieved for alkali magnetometers (see Chapter 5), and correspondingly better sensitivity to the magnetization of the noble gas and hence rotation rate.

Collisional spin destruction from the spin–rotation interaction transfers polarization from the electron spin to the atoms' translational degrees of freedom, causing alkali spin relaxation and putting a fundamental limit on the efficiency of spin-exchange optical pumping [4]. This process therefore limits the maximum nuclear polarization that can be achieved and hence the rotation signal magnitude.

Finally, the light shift induced by the optical pumping light results in an effective magnetic field [51,52]. This effective field varies throughout the cell if the laser beam is not perfectly collimated and if the optical density of the alkali atoms is high. This can lead to broadening and relaxation similar to magnetic-field gradients.

19.4 Two-spin NMR gyroscope

As pointed out in Section 19.1, the magnetic-field stability requirements are greatly relaxed when two NMR isotopes are used in an NMRG. NMR gyroscopes developed in the 1960s and 1970s based on two isotopes demonstrated bias instabilities lower than 0.1°/h. The history of NMR gyroscopes is somewhat masked by commercial and military secrecy, but several reviews of this early work have been published [53–57].

The first two-spin NMRG was based on mercury isotopes [9,58,59]. A simplified diagram of an NMR gyroscope based on mercury is presented in Fig. 19.3. The vapor cell contains ^{199}Hg, ^{201}Hg, and a buffer gas. The Hg nuclear spins are optically pumped and probed with light at 253.7 nm emitted by two ^{204}Hg lamps. Coherent spin precession at the atomic

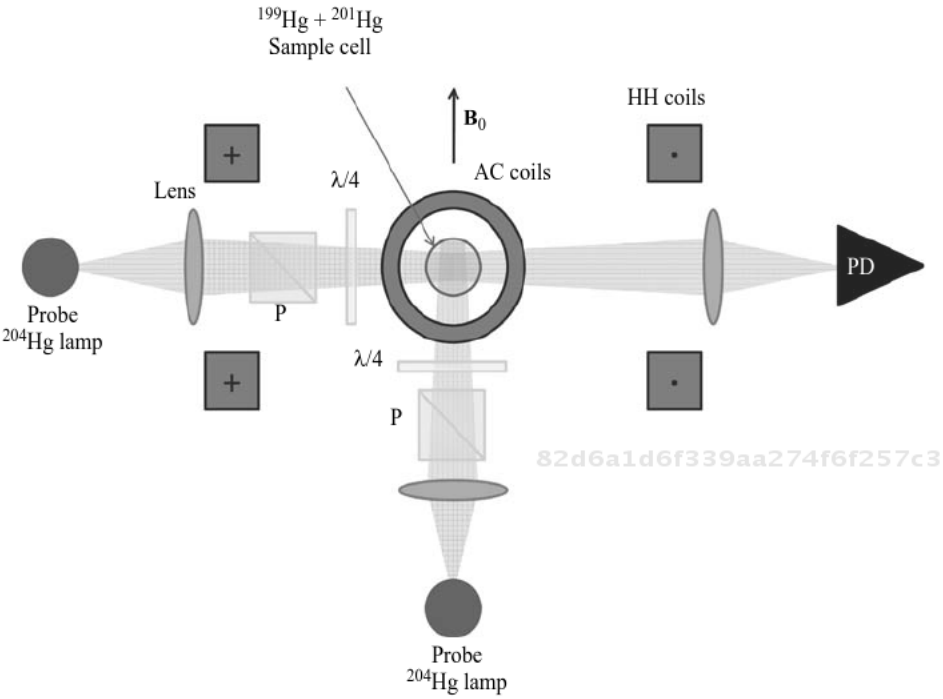

Figure 19.3 A mercury NMRG. A vapor cell contains ^{199}Hg, ^{201}Hg, and some buffer gas. The Hg nuclear spins are optically pumped and probed with light from ^{204}Hg lamps at 253.7 nm that is circularly polarized by polarizers (P) and quarter-wave plates ($\lambda/4$). The 253.7 nm line from the ^{204}Hg lamps overlaps optical pumping transitions in both ^{199}Hg and ^{201}Hg, making ^{204}Hg lamps a convenient light source. A DC bias field $\mathbf{B}_0$ is generated by a pair of Helmholtz coils (HH). Coherent spin precession is generated with applied AC magnetic fields perpendicular to $\mathbf{B}_0$. The Hg spin-precession frequencies are detected as modulations of the probe-beam transmission through the cell as measured by the photodiode (PD).

Larmor frequency is driven by applied AC magnetic fields perpendicular to a static field, $\mathbf{B}_0$. The precession frequency is detected optically as a modulation of the probe-beam transmission [60].

When the NMRG is rotating about the axis of the static field B_0, the measured Larmor frequencies are shifted by the rotation rate Ω:

$$\omega_{199} = \gamma_{199} B_0 + \Omega\,, \tag{19.7}$$

$$\omega_{201} = |\gamma_{201}|\, B_0 - \Omega\,. \tag{19.8}$$

Note that the signs of γ are opposite for ^{199}Hg and ^{201}Hg (they precess in opposite directions; see Table 19.1), so the rotational shifts for the two isotopes have the same magnitude but opposite sign. However, the two Hg isotopes have different magnetic-field shifts, owing to

their different gyromagnetic ratios. Solving Eqs. (19.7) and (19.8) for Ω gives

$$\Omega = \frac{\gamma_{199}\omega_{201} - |\gamma_{201}|\,\omega_{199}}{\gamma_{199} + |\gamma_{201}|}, \tag{19.9}$$

thus the rotation rate can be determined from measurements of ω_{199} and ω_{201}. Note also that the magnetic field can be servoed by stabilizing the sum of the NMR frequencies, since the sum $\omega_{199} + \omega_{201} = (\gamma_{199} + |\gamma_{201}|)\,B_0$ is independent of the rotation rate. When the total magnetic field is servoed by the sum of the NMR frequencies, the rotation rate and angle can be found from the frequency and phase shifts between the signal from one of the NMR isotopes and a reference oscillator [61], which can simplify signal processing. As of the early 1980s, this dual-species approach with Hg had achieved $0.053°/\sqrt{\text{h}}$ for the ARW [53] and a bias instability of 0.02°/h [57].

Spin-exchange optical pumping (SEOP) [4] in mixtures of alkali and noble-gas atoms can also be used to realize NMR gyroscopes based on spin-polarized noble-gas nuclei [10], making it possible to optically pump the alkali atoms with near-infrared lasers or lamps. Beginning in the 1970s, NMR gyroscopes based on noble-gas isotopes were introduced [10, 61, 62]. The alkali atoms that pump the noble-gas nuclei were simultaneously mechanized as an in-cell magnetometer to sense noble-gas nuclear precession. NMR gyroscopes based on ^{129}Xe and ^{131}Xe and spin-exchange optically pumped by Rb achieved a bias instability of 0.01°/h and an ARW of $0.002°/\sqrt{\text{h}}$ [63]. These systems had a total volume of several hundred cubic centimeters per axis of rotation.

19.5 Comagnetometer

Recently, a novel version of an NMR gyroscope based on a potassium–^{3}He comagnetometer was demonstrated that achieved performance comparable to dual species NMR gyroscopes, but with a single nuclear isotope [11]. In this configuration, the K spins act as the rotation sensors, with their response to rotation enhanced by the presence of the ^{3}He and their response to magnetic-field drifts suppressed by the presence of the ^{3}He. The comagnetometer was developed to perform sensitive tests of physics beyond the standard model [64] (see Chapter 18, Sections 18.3 and 18.4).

The comagnetometer consisted of a vapor cell of 2.5 cm diameter containing ~7 amagat of ^{3}He, K metal, and about 20 torr of nitrogen gas to optimize optical pumping by quenching the K excited state. A circularly polarized pump laser beam polarized the K vapor and hence the ^{3}He nuclei through collisions. A diagram of the cell and relevant magnetic fields is shown in Fig. 19.4.

Through the spin-exchange interaction [Eq. (19.5)], the ^{3}He nuclei generate an effective field of order 100 nT as sensed by the K spins. The K effective field as sensed by the ^{3}He is of order 0.1 nT. Therefore the two spin ensembles effectively sit in different magnetic fields. In spite of their vastly different gyromagnetic ratios, the spin-exchange interaction makes it possible for the K electronic spins and the ^{3}He nuclear spins to have nearly the same Larmor frequency, such that their spin dynamics are strongly coupled [65]. The required applied

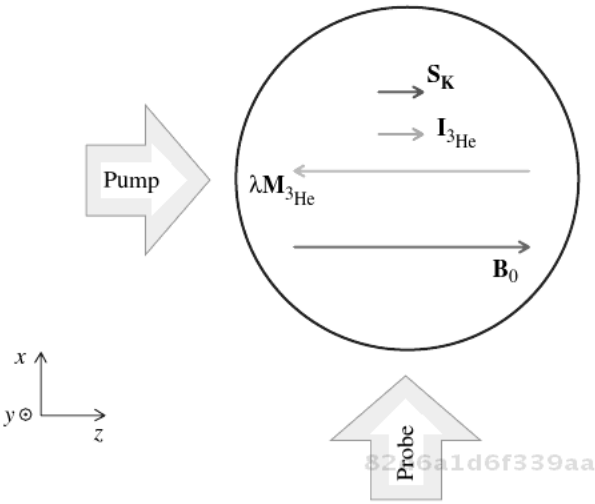

Figure 19.4 Field configuration for the comagnetometer gyroscope. Here $\mathbf{S_K}$ denotes the K electron spin, $\mathbf{I}_{^3\mathrm{He}}$ denotes the ^{3}He nuclear spin, and $\lambda\mathbf{M}_{^3\mathrm{He}}$ is the effective magnetic field felt by the K atoms due to the ^{3}He polarization, where $\lambda = 8\pi\kappa_0/3$. The linearly polarized probe beam detects any K spin projection along the x-axis via the polarization rotation technique. The instrument is sensitive to rotations along the y-axis.

field to reach this regime of strong coupling is nearly equal in magnitude but opposite in direction to the ^{3}He effective field.

In this field configuration, the total field as sensed by the K spins nearly vanishes, and the K–K spin-exchange rate exceeds the K Larmor frequency such that the comagnetometer operates in the spin-exchange-relaxation-free regime [48, 49], thus enhancing the magnetometer sensitivity. The K effective field as sensed by the ^{3}He is large enough to reduce relaxation from magnetic-field gradients [Eq. (19.6)].

The gyroscope signal arises from the x-component of the K polarization that results from a rotation about the y-axis. Because of the strong coupling between the ^{3}He and K spins, the x-component of the K polarization is enlarged by a factor of γ_K/γ_{3He}, which is nearly a factor of 1000.

The comagnetometer configuration reduces the sensitivity of the gyroscope to magnetic field drifts, transients, and gradients since the effective field arising from the ^{3}He magnetization screens the K spins such that they sit in a near-zero magnetic field. For field changes that are slow compared to the ^{3}He Larmor frequency, the ^{3}He polarization adiabatically follows the total field and cancels slow changes in the applied field.

With the K–^{3}He comagnetometer, an ARW of $0.002°/\sqrt{\text{h}}$ and a bias instability of 0.04°/h were achieved. A comagnetometer based on ^{21}Ne might exhibit improvement in instability by an order of magnitude, resulting from its smaller gyromagnetic ratio (1/10 that of ^{3}He).

19.6 Miniaturization

For many applications, the most important issue is not improving performance but, instead, maintaining performance while reducing size, weight, and power. Microfabrication techniques, described in detail in Chapter 7, can allow for substantial reductions in these instrument parameters. Instrument cost can also be reduced, especially if batch fabrication processes are used and volume manufacturing is possible. For some applications, NMR gyroscopes have the potential advantage over micromachined spinning or vibratory gyroscopes in that they contain no moving parts and they are relatively insensitive to vibrations.

The recent level of activity in NMR gyroscopes is indicated by the number of patents that have emerged [20, 66–71] – most of which are related to miniaturization. Reference [66] is a scheme for using batch processing to develop a chip-scale atomic gyroscope. To enable low power consumption, the proposed device uses permanent magnets and low-power vertical-cavity surface emitting lasers. Two patents pertain to cell fabrication techniques [67, 68]. One patent describes ways to pattern electrical conductors to mostly cancel stray fields that arise from the cell heaters [69]. Two patents describe solenoid geometries that improve magnetic-field uniformity [70, 71]. One patent describes instrument geometries that make use of a diverging laser beam to simultaneously pump and probe the atoms and reduce common-mode noise through differential detection [72].

Wafer-level arrays of glass-blown spherical microcells have been developed [73, 74], as have methods to deposit mirrors onto angled cell walls etched in silicon [75, 76]. Several miniaturized NMR gyroscope components and integration methods were used for an NMR gyroscope prototype described in [77].

An advantage of miniaturization is that magnetic shielding is less expensive and works much better for smaller instruments [78]. A disadvantage of miniaturization is that cell-wall effects become much stronger, which results in larger NQR frequency shifts and shorter spin lifetimes.

In spite of the reduced spin lifetimes, the performance of microfabricated prototypes is approaching the requirements for the navigation of commercial aircraft [79]. So far, an ARW of $0.01°/\sqrt{\text{h}}$ and a bias instability of $0.05°/\text{h}$ has been demonstrated in a 6-cm^3 physics package. Work is ongoing to reduce the power and size requirements while continuing to improve the performance.

19.7 Conclusion

NMR gyroscopes are a relatively old idea that is experiencing a revival – partly because of their potential for miniaturization and low-cost fabrication, and partly because of their potential for use in demanding navigation applications. We have presented a review of the basic physics involved with NMR gyroscopes, and have summarized the published performance results.

Acknowledgments

Enlightening discussions with M. Bulatowicz, M. Larsen, and M. V. Romalis are gratefully acknowledged. This article is a contribution of the US government, not subject to US copyright.

References

[1] H. Goldstein, *Classical Mechanics* (Addison-Wesley, New York, 1950).
[2] R. K. Harris *et al.*, Pure Appl. Chem. **73**, 1795 (2001).
[3] P. G. Groves, *Principles of GNSS, Inertial, and Multisensor Integrated Navigation Systems* (Artech House, Norwood, MA, 2008).
[4] T. G. Walker and W. Happer, Rev. Mod. Phys. **69**, 629 (1997).
[5] I. A. Greenwood and J. H. Simpson, *Proceedings of the IEEE 1977 National Aerospace and Electronics Conference (NAECON77)*, 1246 (1977).
[6] J. Kitching, S. Knappe, and E. A. Donley, IEEE Sensors **11**, 1749 (2011).
[7] B. D. Leete, United States Patent 2,720,625 (1955).
[8] A. Hansen, United States Patent 2,841,760 (1958).
[9] J. H. Simpson, J. T. Fraser, and I. A. Greenwood, IEEE Trans. Aerospace **1**, 1107 (1963).
[10] E. Kanegsberg, *Proceedings of the 2nd Digital Avionics Systems Conference*, 40 (1977).
[11] T. W. Kornack, R. K. Ghosh, and M. V. Romalis, Phys. Rev. Lett. **95**, 230801 (2005).
[12] W. Happer, E. Miron, S. Schaefer, D. Schreiber, W. A. van Wijngaarden, and X. Zeng, Phys. Rev. A **29**, 3092 (1984).
[13] R. J. Knize, Z. Wu, and W. Happer, Adv. Atomic Mol. Phys. **24**, 223 (1987).
[14] G. D. Cates, R. J. Fitzgerald, A. S. Barton, P. Bogorad, M. Gatzke, N. R. Newbury, and B. Saam, Phys. Rev. A **45**, 4631 (1992).
[15] T. G. Walker, Phys. Rev. A **40**, 4959 (1989).
[16] R. M. Herman, Phys. Rev. **137**, A1062 (1965).
[17] R. L. Gamblin and T. R. Carver, Phys. Rev. **138**, A946 (1965).
[18] B. C. Grover, Phys. Rev. Lett. **40**, 391 (1978).
[19] S. R. Schaefer *et al.*, Phys. Rev. A **39**, 5613 (1989).
[20] E. Kanegsberg, United States Patent 7,282,910 B1 (2007).
[21] C. Cohen-Tannoudji, J. Phys.-Paris **24**, 653 (1963).
[22] C. H. Volk, J. G. Mark, and B. C. Grover, Phys. Rev. A **20**, 2381 (1979).
[23] P. A. Heimann, Phys. Rev. A **23**, 1204 (1981).
[24] P. A. Heimann, I. A. Greenwood, and J. H. Simpson, Phys. Rev. A **23**, 1209 (1981).
[25] T. M. Kwon, J. G. Mark, and C. H. Volk, Phys. Rev. A **24**, 1894 (1981).
[26] Z. Wu, W. Happer, and J. M. Daniels, Phys. Rev. Lett. **59**, 1480 (1987).
[27] Z. Wu, S. Schaefer, G. D. Cates, and W. Happer, Phys. Rev. A **37**, 1161 (1988).
[28] Z. Wu, W. Happer, and J. M. Daniels, Phys. Rev. A **42**, 2774 (1990).
[29] R. Butscher, G. Wäckerle, and M. Mehring, J. Chem. Phys. **100**, 6923 (1994).
[30] R. Butscher, G. Wäckerle, and M. Mehring, Chem. Phys. Lett. **249**, 444 (1996).
[31] S. K. Lamoreaux, J. P. Jacobs, B. R. Heckel, F. J. Raab, and E. N. Fortson, Phys. Rev. Lett. **57**, 3125 (1986).
[32] S. K. Lamoreaux, J. P. Jacobs, B. R. Heckel, F. J. Raab, and E. N. Fortson, Phys. Rev. A **39**, 1082 (1989).

[33] S. Appelt, G. Wäckerle, and M. Mehring, Phys. Rev. Lett. **72**, 3921 (1994).
[34] E. A. Donley, J. L. Long, T. C. Liebisch, E. R. Hodby, T. A. Fisher, and J. Kitching, Phys. Rev. A **79**, 013420 (2009).
[35] X. Zeng, E. Miron, W. A. Van Wijngaarden, D. Schreiber and W. Happer, Phys. Lett. **96A**, 191 (1983).
[36] A. T. Nicol, Phys. Rev. B **29**, 2397 (1984).
[37] W. A. Fitzsimmons and G. K. Walters, Phys. Rev. Lett. **19**, 943 (1967).
[38] L. D. Schearer and G. K. Walters, Phys. Rev. **139**, A1398 (1965).
[39] G. D. Cates, S. R. Schaefer, and W. Happer, Phys. Rev. A **37**, 2877 (1988).
[40] M. V. Romalis and G. D. Cates, Phys. Rev. A **58**, 3004 (1998).
[41] K. F. Stupic, Z. I. Cleveland, G. E. Pavlovskaya, and T. Meersmann, J. Magn. Reson. **208**, 58 (2011).
[42] D. Brinkmann, E. Brun, and H. H. Staub, Helvetica Phys. Acta **35**, 431 (1962).
[43] R. K. Ghosh and M. V. Romalis, Phys. Rev. A **81**, 043415 (2010).
[44] N. R. Newbury, A. S. Barton, G. D. Cates, W. Happer, and H. Middleton, Phys. Rev. A **48**, 4411 (1993).
[45] W. Happer, Rev. Mod. Phys. **44**, 169 (1972).
[46] W. Happer and H. Tang, Phys. Rev. Lett. **31**, 273 (1973).
[47] W. Happer and A. C. Tam, Phys. Rev. A **16**, 1877 (1977).
[48] J. C. Allred, R. N. Lyman, T. W. Kornack, and M. V. Romalis, Phys. Rev. Lett. **89**, 130801 (2002).
[49] I. K. Kominis, T. W. Kornack, J. C. Allred, and M. V. Romalis, Nature **422**, 596 (2003).
[50] I. M. Savukov and M. V. Romalis, Phys. Rev. A **71**, 023405 (2005).
[51] W. Happer and B. S. Mathur, Phys. Rev. **163**, 12 (1967).
[52] C. Cohen-Tannoudji and J. Dupont-Roc, Phys. Rev. A **5**, 968 (1972).
[53] F. A. Karwacki, J. Inst. Navigation **27**, 72 (1980).
[54] K. F. Woodman, P. W. Franks, and M. D. Richards, J. Navigation **40**, 366 (1987).
[55] K. Liu, W. Zhang, W. Chen, K. Li, F. Dai, F. Cui, X. Wu, G. Ma, and Q. Xiao, J. Micromech. Microeng. **19**, 113001 (2009).
[56] E. A. Donley, *IEEE Sensors, Waikaloa, HI*, 17 (2010).
[57] M. S. Goldstein, I. A. Greenwood, M. M. Kuritsky, H. Lerman, J. E. McCarthy, T. Shanahan, M. Silver, and J. H. Simpson, Proc. IEEE **71**, 1156 (1983).
[58] J. H. Simpson, Astronaut. Aeronaut. **2**, 42 (1964).
[59] D. S. Bayley, I. A. Greenwood, and J. H. Simpson, United States Patent 3,778,700 (1973).
[60] H. G. Dehmelt, Phys. Rev. **105**, 1924 (1957).
[61] B. C. Grover, E. Kanegsberg, J. G. Mark, and R. L. Meyer, United States Patent 4,157,495 (1979).
[62] E. Kanegsberg, Proc. SPIE **157**, 73 (1978).
[63] L. K. Lam, E. Phillips, E. Kanegsberg, and G. W. Kamin, Proc. SPIE **412**, 272 (1983).
[64] J. M. Brown, S. J. Smullin, T. W. Kornack, and M. V. Romalis, Phys. Rev. Lett. **105**, 151604 (2010).
[65] T. W. Kornack and M. V. Romalis, Phys. Rev. Lett. **89**, 253002 (2002).
[66] H. C. Abbink, E. Kanegsberg, and R. A. Patterson, United States Patent 7,239,135 (2007).
[67] H. C. Abbink, E. Kanegsberg, K. D. Marino, and C. H. Volk, United States Patent 7,292,031 (2007).
[68] H. C. Abbink, W. P. Debley, C. E. Geosling, D. K. Sakaida, and R. E. Stewart, United States Patent 7,292,111 (2007).

[69] M. Bulatowicz, United States Patent 2009/0316753 A1 (2009).
[70] M. Bulatowicz, United States Patent 2010/0194506 A1 (2010).
[71] M. Bulatowicz, United States Patent 2011/0247414 A1 (2011).
[72] J. Kitching, E. A. Donley, E. Hodby, A. Shkel, and J. Eklund, United States Patent 7,872,473 (2011).
[73] E. J. Eklund, A. M. Shkel, S. Knappe, E. Donley, and J. Kitching, Sensor Actuat. A **16**, 232 (2007).
[74] E. J. Eklund, A. M. Shkel, S. Knappe, E. Donley, and J. Kitching, Sensor Actuat. A **143**, 175 (2008).
[75] M. A. Perez *et al.*, Sensor Actuat. A **154**, 295 (2009).
[76] M. A. Perez, J. Kitching, and A. M. Shkel, Sensor Actuat. A **155**, 23 (2009).
[77] E. J. Eklund, Ph.D. Thesis, University of California, Irvine (2008).
[78] E. A. Donley, E. Hodby, L. Hollberg, and J. Kitching, Rev. Sci. Instrum. **78**, 083102 (2007).
[79] M. Larsen, *42nd Annual Meeting of the APS Division of Atomic, Molecular, and Optical Physics* (Atlanta, GA, June 13-17, 2011).